JOURNAL OF THERMOPHYSICS AND HEAT TRANSFER
Vol. 22, No. 4, October–December 2008

Flow Visualization and Heat Transfer Characteristics for Sphere-Packed Pipes

Kazuhisa Yuki,* Masumi Okumura,† Hidetoshi Hashizume,‡ and Saburo Toda§
Tohoku University, Miyagi 980-8579, Japan
Neil B. Morley¶
University of California, Los Angeles,
Los Angeles, California 90095-1597
and
Akio Sagara**
National Institute for Fusion Science, Toki 509-5292, Japan

DOI: 10.2514/1.30141

Particle image velocimetry visualization to identify the complex flow structures in a sphere-packed pipe is carried out by using a matched refractive-index method with a sodium iodide solution as the working fluid. The following three flows were confirmed as representative flow structures in the pipe: a meandrous bypass flow with a high-flow velocity due to the wall effect, two pairs of unstable twin vortices accompanied by a strong impinging flow to the pipe wall, and a spouting flow from the central area of the pipe. In an experiment on heat transfer using water as the working fluid, the wall-temperature distribution is measured with thermocouples and infrared thermography, which makes clear a relation between the flow structures and the local heat transfer performance. Though an area with a high wall temperature is formed by the flow stagnation located at a contact point between the sphere and the heating wall, the colliding effect of the high velocity and of the meandrous bypass flow with the spheres significantly affects the heat transport from the stagnation areas. On the other hand, the heat transfer performance is quite high in a large gap area between the upstream and downstream spheres because of the influence of the strong impinging flow and the vortices that are both induced by the meandrous bypass flow.

Nomenclature

c_p	=	specific heat at a constant pressure
D	=	inner diameter of a circular pipe
d	=	sphere diameter
H	=	quantity of heat generation per unit volume
h	=	heat transfer coefficient
k	=	thermal conductivity of a circular pipe in the heat transfer experiment
M	=	mass flow rate
Pr	=	Prandtl number
p	=	pressure of the fluid
$Q(z)$	=	quantity of heat that the fluid has received from the inlet up to location z in a streamwise direction.
q	=	heat flux input
R	=	inradius of a circular pipe
Re_d	=	Reynolds number based on sphere size
Re_D	=	Reynolds number based on circular-pipe diameter
r	=	location in a radial direction
r_i, r_o	=	inradius and circumradius of a circular pipe
T_b	=	bulk temperature of the fluid
T_w	=	inner wall temperature of a circular pipe
T'_w	=	outer wall temperature of a circular pipe
U	=	inlet velocity (superficial velocity in a sphere-packed pipe)
U_p, V_p	=	root mean square of the velocity fluctuations in the horizontal and vertical directions in a visualizing section
u, v	=	mean velocities in the horizontal and vertical directions in a visualizing section
z	=	location in a streamwise direction
δ	=	light path difference
ν	=	kinematic coefficient of viscosity

Presented as Paper 5426 at the 9th AIAA/ASME Joint Thermophysics and Heat Transfer Conference, San Francisco, CA, 5–8 June 2006; received 3 May 2007; revision received 6 December 2007; accepted for publication 10 December 2007.

*Assistant Professor, Department of Quantum Science and Energy Engineering, Sendai; kyuki@qse.tohoku.ac.jp.
†Graduate, Department of Quantum Science and Energy Engineering, Sendai; moku@karma.qse.tohoku.ac.jp.
‡Professor, Department of Quantum Science and Energy Engineering, Sendai; hidetoshi.hashizume@qse.tohoku.ac.jp.
§Professor Emeritus, Department of Quantum Science and Energy Engineering, Sendai; saburo.toda3727@qse.tohoku.ac.jp.
¶Associate Professor, Mechanical and Aerospace Engineering Department; morley@fusion.ucla.edu.
**Professor, Fusion and Advanced Technology System Division; sagara.akio@LHD.nifs.ac.jp.

I. Introduction

NUCLEAR fusion reactors currently under research and development are generally classified as two types, a solid breeder reactor and a liquid breeder reactor, according to the breeding method for tritium, which is used as fuel for the fusion reaction. The liquid breeding method has the advantage of a simplified reactor system, because it enables a self-cooling system whereby the breeder materials, including Li, can work as a coolant for plasma facing components. In the heliotron-type fusion reactor force-free helical reactor (FFHR) promoted by the National Institute for Fusion Science (NIFS), the greatest benefit of the blanket design adopting the spectral shifter [1] that Sagara and Imagawa proposed is that it is basically maintenance free for 30 years, with the emphasis on blanket maintainability. However, one downside to this approach is that the heat load on a first wall shoots up higher than ever before. High heat removal of approximately 1 MW/m^2 on heat flux, by single-phase flow, is therefore a significant research and development issue that holds the key of realizing this blanket design.

On another front, the proposition of the high-temperature molten salt FLiBe as a working fluid for FFHR holds some advantages, which are as follows: a high heat capacity, a low electric conductivity, and a low vapor pressure. However, the heat transfer performance of FLiBe, which is a high Pr number fluid, is inferior to such liquid metals as Li or LiPb, and so the application of a heat transfer enhancement is absolutely essential. Furthermore, when it is used as the cooling technology for the commercial-type fusion power reactor, it is not enough to simply ensure coolability with some margins. In setting up a long-term nuclear power plant, it is important to develop a heat transfer promoter that can withstand neutron load and maintain chemical compatibility between the structural materials and the high-temperature molten salt FLiBe and can also lead to a beneficial effect on soundness, profitability, and maintainability. Additionally, heat removal at a lower flow rate is desirable when taking into account a magnetohydrodynamic (MHD) pressure drop and electrolysis [2] that becomes problematical for the molten salt flow under a strong magnetic field. Erosion could also emerge as a problem in a plant as large as a nuclear power plant.

To develop the heat transfer promoter for the high Pr number fluid FLiBe in accordance with the strict conditions, the authors have focused on a sphere-packed pipe (SPP) as a basic heat transfer promoter. As Fig. 1 shows, the SPP involves comparatively large metal spheres inside the pipe and has the characteristic of being able to easily change to a turbulent regime in comparison with the case of a single sphere, as well as the increase of the heat transfer area. At the same time, the SPP can also heighten the effect of neutron multiplication required in the fuel generation with the selection of Be or Pb as materials for the spheres. The SPP research should ultimately lead to the development of advanced SPP, which can dramatically reduce heat resistance at a contact point between the sphere and the heating wall and improve the existing fin effect by putting riblets or dimples on the sphere surface as a means of drag reduction. Against this background, the authors have evaluated the fundamental heat transfer performance of the SPPs using the Tohoku–NIFS Thermofluid loop, which can be regarded as the largest forced circulation loop for high-temperature molten salt in the world [3,4]. Moreover, to figure out a relation between the pressure-drop/heat transfer characteristics and the inside flow structures in the SPP regularly packed spheres, the pressure-drop characteristics were evaluated first using water as the working fluid [5]. This experiment showed that the SPP with a certain sphere size led to a greater reduction in the pressure drop than that predicted by Ergun's correlation [6] for a packed bed flow, and the pressure drop almost corresponds rather to a drag model [7]. On the other hand, although numerous heat transfer experiments and simulations have been conducted, in particular with the packed bed that uses a much smaller sphere than the characteristic length of the pipe, fewer studies have been carried out with larger spheres. Fand et al. have constructed correlations for the pressure-drop characteristics and the average heat transfer coefficients of the SPP flows with relatively large, irregularly packed glass spheres [8–11]. However, as far as the authors know, nothing is known about a relationship between the local heat transfer rate and the inside flow structures of the SPP.

The purpose of this research is, first, to evaluate the flow structures in the sphere-packed pipe with comparatively large spheres by particle image velocimetry (PIV), using a matched refractive-index method that uses a sodium iodide solution as the working fluid. Second, a relationship between the local heat transfer performance and the flow structures is considered by conducting heat transfer experiments focusing on the wall-temperature distribution. This research is also aimed at clarifying some engineering issues for the SPP technology that result from the high Pr number fluid.

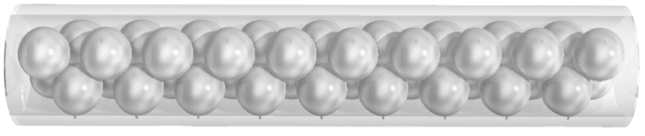

Fig. 1 Sphere-packed pipe (each sphere is a half-dimension of the circular-pipe diameter).

II. Visualization and Heat Transfer Experiments on a Sphere-Packed Pipe Flow

A. PIV Visualization Using a Matched Refractive-Index Method

1. *Refractive-Index Adjustment of the Sodium Iodide Solution*

Where a three-dimensional flow structure around obstacles inside a pipe, such as the SPP, is visualized by a PIV technique, it is extremely difficult to grasp the whole flow structure even when transparent spheres are used, because the difference of the refractive index between the working fluid and the sphere causes distortion in the image. Therefore, it is necessary to match the refractive index of the working fluid with that of the sphere material. This research employs a sodium iodide (NaI) solution, which is easy to handle and chemically stable, as the working fluid. This solution is deliberately chosen to be able to adjust the refractive index of the working fluid to that of the acrylic sphere with an index of 1.49. Normally, the refractive index of a solution is not so sensitive to temperature change, and so the refractive index of the NaI solution is adjusted by changing its concentration. Figure 2 shows a light path difference caused by refraction, in which a YAG laser used in the PIV measurement is irradiated to an acrylic cylinder 30 mm in diameter fixed at the center of a 10-cm square acrylic box filled with NaI solution at 30 °C. The light path difference, δ, is measured at a location 660 mm from the back of the cylinder. The difference decreases with the increase in the NaI concentration and reaches zero at 61.6 wt%. That means that the refractive index of the NaI solution completely corresponds with that of the acrylic cylinder at this concentration. In actual visualization experiments, a refractive index at this concentration under visible light, which is 1.485, was always checked by using a portable refractometer before each experiment, because the change in the refractive index might be caused by the deposition of NaI crystals onto the pipe wall and/or by volatilization from the solution.

2. *PIV Measurement with Fluorescence Particles*

The PIV used in this experiment is a double-pulse YAG laser system manufactured by Japan Laser Corporation. The laser output is 25 mJ at 532 nm, and the maximum oscillatory frequency is 30 Hz. In the PIV measurement, a time series of tracer particles' images in a sheet laser is taken with a high-speed camera and then a two-dimensional flow structure is quantitatively visualized from the movement of the tracer particles. The time interval of the double pulse and the tracer concentration is adjusted depending on the flow conditions. To process the obtained particle images, a cross-correlation scheme is adopted to get spatially dense velocity information. Furthermore, melamine fluorescent resin particles 1–20 μm diameter are used as the tracer particles. The specific gravity of the NaI solution at the aforementioned concentration is relatively close to that of this tracer, and so the buoyancy influence can be ignored. When this fluorescent particle is irradiated with the

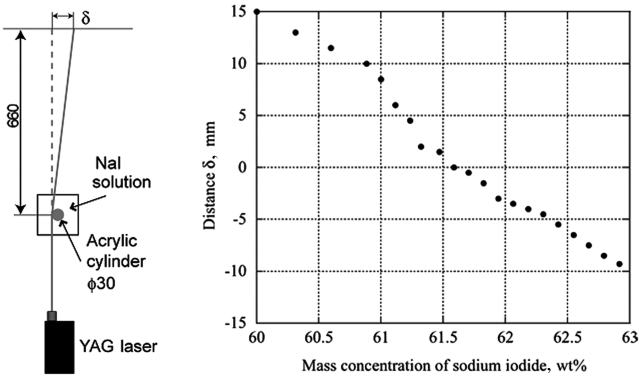

Fig. 2 Matched refractive-index experiment using NaI.

YAG laser, it causes excitation in the fluorescent agent, which emits light of 580 nm in wavelength. By taking only this newly emitted light into a CCD camera with an attached filter lens, it makes it possible to obtain a clearer particle image than the usual tracer image, because the diffused reflection light of the laser observed on the pipe wall surface and on the acrylic sphere surface can be removed simultaneously.

3. *Experimental Apparatus and Details of the Test Section*

Figure 3 shows a diagram of the apparatus for the visualization experiment under isothermal conditions. The apparatus consists of the following components: a circulating pump, a flow rate measuring section, a flow-straightened section, a test section, a bag filter, and a mixing tank. All piping materials and components have been made of polyvinyl chloride or acrylic materials, etc., which coexist in a stable state with the NaI solution. The magnetic pump circulates the working fluid inside the loop, and its maximum flow rate under sphere-unpacked conditions is approximately 200 l/ min. The flow rate of the working fluid is adjusted by valves: two valves located between the magnetic pump and the flow rate measuring section and a valve of a bypass line that directly returns to the mixing tank from the magnetic pump.

A turbine flowmeter or an ultrasonic Doppler velocimeter is used to measure the flow rate. The mixing tank has the following functions: injection of tracer particles, deaeration of bubbles existing in the fluid, and heat exchange to control the fluid temperature. The section upstream of the test section has a flow straightener with a honeycomb structure consisting of stainless steel pipes, which straightens and counteracts a swirling flow formed in the bend upstream. The bag filter is a polypropylene-made cartridge with strong corrosion resistance that separates the tracer particles from the NaI solution.

Figure 4 shows a detailed view of the visualization test section. The test section is an acrylic vertical riser pipe with $D = 56$ mm as the inner diameter and 670 mm as the length. The visualizing area is located at $8.2D$ (460 mm) downstream from an inlet of the test section, where a fully developed flow is anticipated. In addition, there is a rectangular jacket surrounding the test section to reduce the image distortion resulting from the geometry of the circular pipe. The NaI solution is also filled into the jacket. To visualize the flowfield in the lateral cross section of the circular pipe, an acrylic observation window is attached to the upper part of the test section. Both sides upstream and downstream of the test section have a Bourdon tube pressure gauge to measure the pressure drop.

4. *Sphere Packing Structure and Experimental Conditions*

Figure 5 shows the packing structure of the acrylic spheres. The sphere size prepared for this research is $D/2.0$ (27.6 mm) in diameter, and 68 spheres can be packed in the test section with a

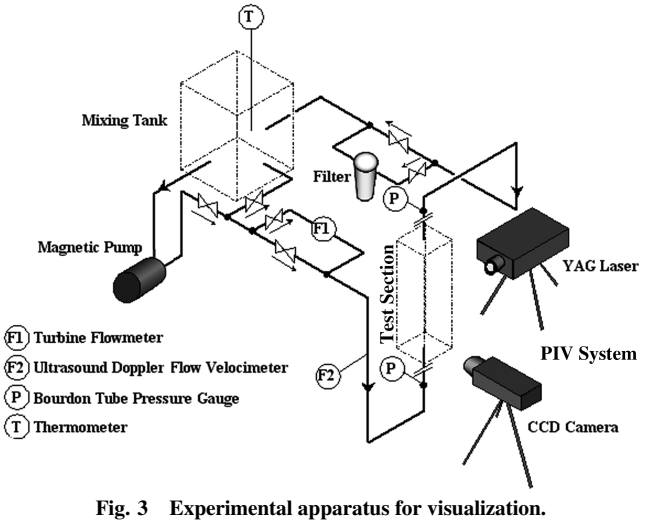

Fig. 3 Experimental apparatus for visualization.

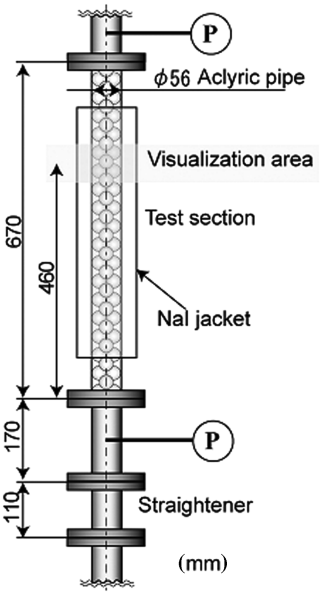

Fig. 4 Test section.

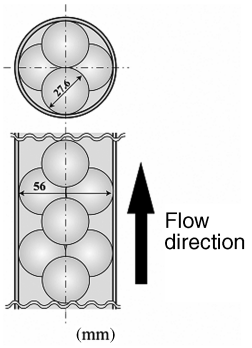

Fig. 5 Packing structure.

porosity of 0.548. An acrylic baffle plate set between the flanges, which exist at the inlet and outlet of the test section, fixes the acrylic spheres.

The temperature of the NaI solution is 30 °C, and the visualization of the flowfield is conducted at three Reynolds numbers ($Re_d = Ud/\nu$) of 800, 2000, and 4900, based on the sphere diameter, d, and mean inlet velocity U. The mean inlet velocity, which is equivalent to the superficial velocity in the SPP, is 0.0376, 0.0940, and 0.230 m/s, respectively. From the data of the friction factor, Varahasamy and Fand have classified the SPP pipe flow with $D/d > 1.4$ into the turbulent regime ($Re_d > 120$), the Forchheimer regime ($5 < Re_d < 80$), and the Darcy regime ($Re_d < 2.3$) [11]. In this sense, the flow conditions in this research could be in the turbulent regime. This fact was also confirmed by the authors' experiments [5].

B. Visualization of Wall-Temperature Distribution and Evaluation of the Local Heat Transfer Coefficient

1. *Experimental Apparatus and Details of the Test Section*

To clarify how the flow structures in the SPP contribute to the local heat transfer characteristics, heat transfer experiments with electrical heating of a circular pipe are performed to measure the wall-temperature distribution by means of thermocouples and infrared thermography. The experiment is carried out by using a boiling bubble visualizing facility [12] at Tohoku University, and its test section is exchanged for the one to be described herein. To ensure consistency with the visualization experiment, the geometries of the test circular pipe, such as the inner diameter and the length, are identical. In addition, this experiment uses water as the working fluid

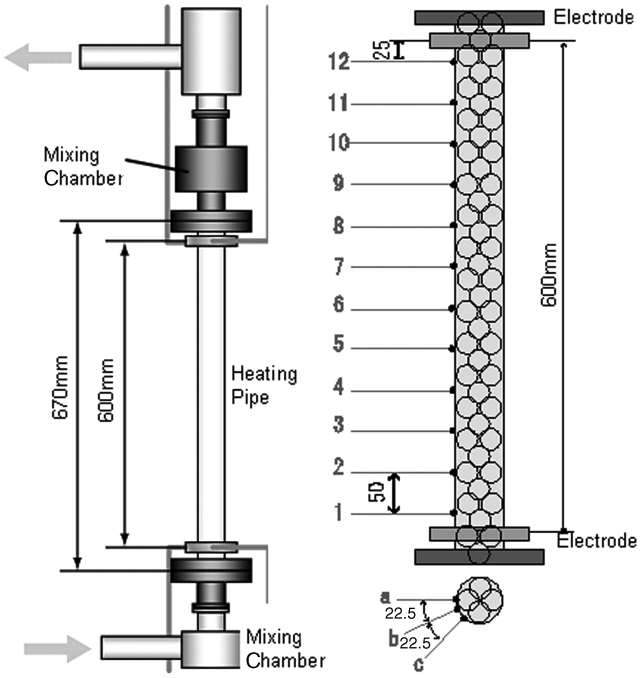

Fig. 6 Test section and the locations of thermocouple for the heat transfer experiment.

because an NaI solution with high electrical conductivity is not appropriate for an experiment using electrical heating. (See Nematollahi et al. [12] for details of each component of the facility.)

The left-hand side of Fig. 6 shows the details of the test section, which is composed of the test circular pipe and the mixing chambers. The circular pipe is a SUS304-made vertical riser pipe 56 mm in inner diameter, 0.5 mm in thickness, and 670 mm in length that is uniformly and electrically heated by an ac power supply [maximum 60 kVA (up to 2000A)]. The acrylic spheres are packed inside the pipe with an identical alignment to that of the visualization experiment. Acrylic thermal conductivity is 0.17–0.25 W/(mK), which is much lower than that of water (0.61 W/(mK) at 30 °C). Therefore, the point-contact heat conduction from the stainless pipe to the acrylic sphere can be ignored or, in other words, the wall-temperature distribution is affected mainly by the convective heat transfer. As shown on the right-hand side of Fig. 6, copper electrodes for the joule heating are attached to the test pipe. The length of the heating region is 600 mm and electrical resistance in this region is 4.77 mΩ. A heat insulator is wrapped around the test section to reduce heat loss to the exterior. It was confirmed that at a wall temperature of 60° the heat loss to the atmosphere and the axial directions of the test pipe was below 1% of the thermal dose in the

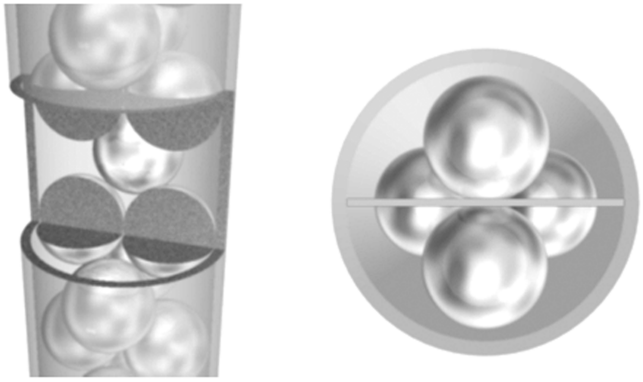

Fig. 7 Visualizing section: S_1.

heat transfer experiments. Inside the mixing chambers upstream and downstream of the test pipe, inlet and outlet bulk temperatures are measured with several K types of sheathed thermocouples 1.0 mm in diameter (the uncertainty is within ±0.75%). In particular, the mixing chamber located downstream has several optimized baffle plates to make uniform the temperature distribution of fluid after the heating region.

2. Wall-Temperature Measurement and Data Analysis

To obtain more accurate outer wall temperatures, 50 μm of thin K-type thermocouples with an uncertainty of ±0.5% are attached onto the outer wall of the test circular pipe with a film tape. The right-hand side of Fig. 6 shows the locations of the thermocouples. Twelve locations are selected at intervals of 50 mm in the axial direction and three thermocouples are attached at intervals of 22.5 deg angles in the circumferential direction at each axial location so that, in total, 36 thermocouples are attached. These locations are selected by taking into account the periodicity and symmetry of the sphere-packed structure. A computer saves the temperature data for three minutes in a steady state through a data logger whose loading interval and uncertainty are 1 s and ±0.025% full scale, respectively. Additionally, infrared thermography is used to visualize the whole distribution of the outer wall temperature to make it easier to discuss the relation between the flow structures inside the SPP and the local heat transfer performance. In this case, the heat insulator is temporarily detached. The infrared thermography equipment is TVS-2200 manufactured by Japan Avionics Corporation, with a time resolution of 30 flames per second and a maximum sensitivity of 0.01°C. The thermal imagery is outputted in the form of 256-color-tone images and binary data.

The following cooling law gives the local heat transfer coefficients under the conditions of the uniform heat flux input q[W/m^2].

$$h_l = q/(T_w - T_b) \tag{1}$$

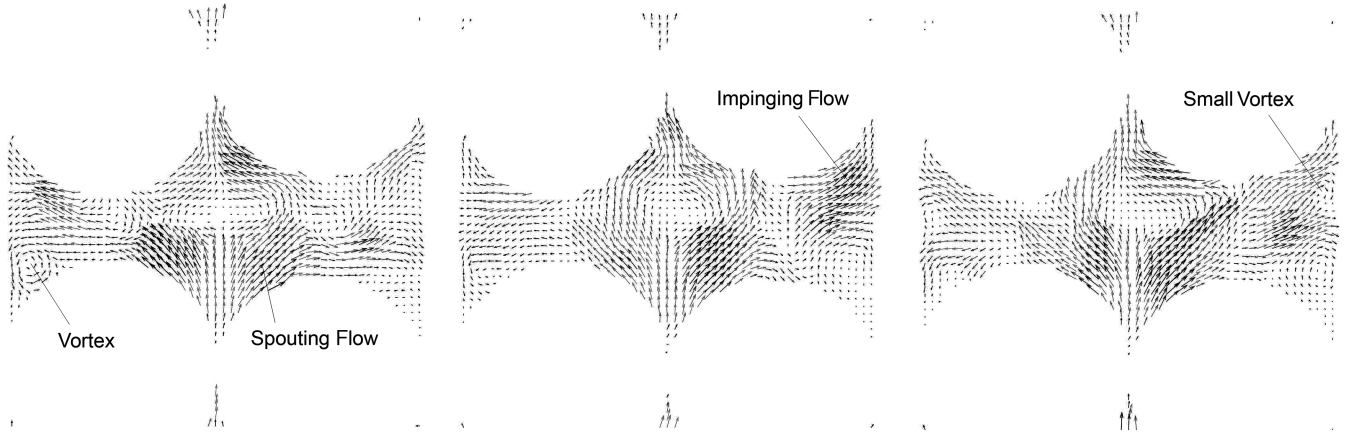

Fig. 8 A time series of flowfields in section S_1 (Re_d = 800, time interval = 0.07 s).

Here, T_w is an inner wall temperature of the circular pipe and T_b is a bulk temperature of fluid calculated from the enthalpy increase, which is given by the following equation:

$$T_b(z) = T_{\text{in}} + Q(z)/(c_p M) \tag{2}$$

In this equation, T_{in} is an inlet bulk temperature, M is a mass flow rate (kg/s), and c_p is a specific heat at constant pressure. Then, $Q(z)$ is the quantity of heat that the fluid has received from the inlet up to the axial location z.

The inner wall temperature, T_w, in Eq. (1) is estimated from the solution of a one-dimensional equation of heat conduction in a radial direction in the cylindrical coordinate system as follows:

$$T_w = \frac{H}{2k}\left(r_o^2 \ln\left(\frac{r_i}{r_o}\right) - \frac{1}{2}\left(r_i^2 - r_o^2\right)\right) + T'_w \tag{3}$$

Here, H is the quantity of heat generation per unit volume, T'_w indicates the outer wall temperature measured by the thermocouple, and k is the thermal conductivity of the circular pipe. In addition, r_i and r_o are the inner radius and outer radius, respectively. Although the heat loss from the heating pipe is very small as already mentioned, H is calculated from Eq. (2) using both the inlet and outlet temperatures to apply a more accurate thermal dose to Eq. (3).

The heat transfer experiments are conducted under a wide range of flow conditions, including the same particle Reynolds number conditions of $Re_d = 800$, 2000, and 4900 as those of the flow visualization experiments, to compare the flow structure obtained by the PIV with the aforementioned heat transfer coefficient data. The inlet temperature is 25°C. Adjusting the current value controls the thermal dose, and the current value is basically set to three patterns, 500, 700, and 900A, with an uncertainty of ±0.25%. However, the data obtained under the conditions that generate natural convection are ruled out when evaluating the heat transfer performance. The uncertainty of the value of the heat transfer coefficient is within 9.0%.

III. Flow Structures in a Sphere-Packed Pipe

A. Flow Structures in a Central Longitudinal Section

First, a central longitudinal section S_1, shown in Fig. 7, is visualized. Figure 8 shows a time series of the flowfields at the lowest Re number of $Re_d = 800$. The color gradation in the grayscale image corresponds to an absolute value of the flow velocity, which means that the flow velocity becomes higher as gray turns to black. The matched refractive-index method makes it possible for the flowfield in the central area of the pipe, which is usually impossible to see, to be successfully and vividly visualized. The whole flowfield fluctuates intensely and is extremely unsteady. To discuss the flowfield more qualitatively, the time-averaged flowfield is shown in Fig. 9a. This clearly shows that a high-velocity flow spouting from upstream of a central area A (spouting flow, hereafter) is pushed back toward the center area again from around the middle of the center area and the wall. Furthermore, judging from the instantaneous flowfields together, a flow toward the pipe wall, which is considered as a part of a wake, forms a strong impinging flow to the pipe wall. After this impingement, a backward flow in the upstream direction forms a circular vortex in the area B between the sphere and the wall. It can be also confirmed that there exists a small circular vortex behind the

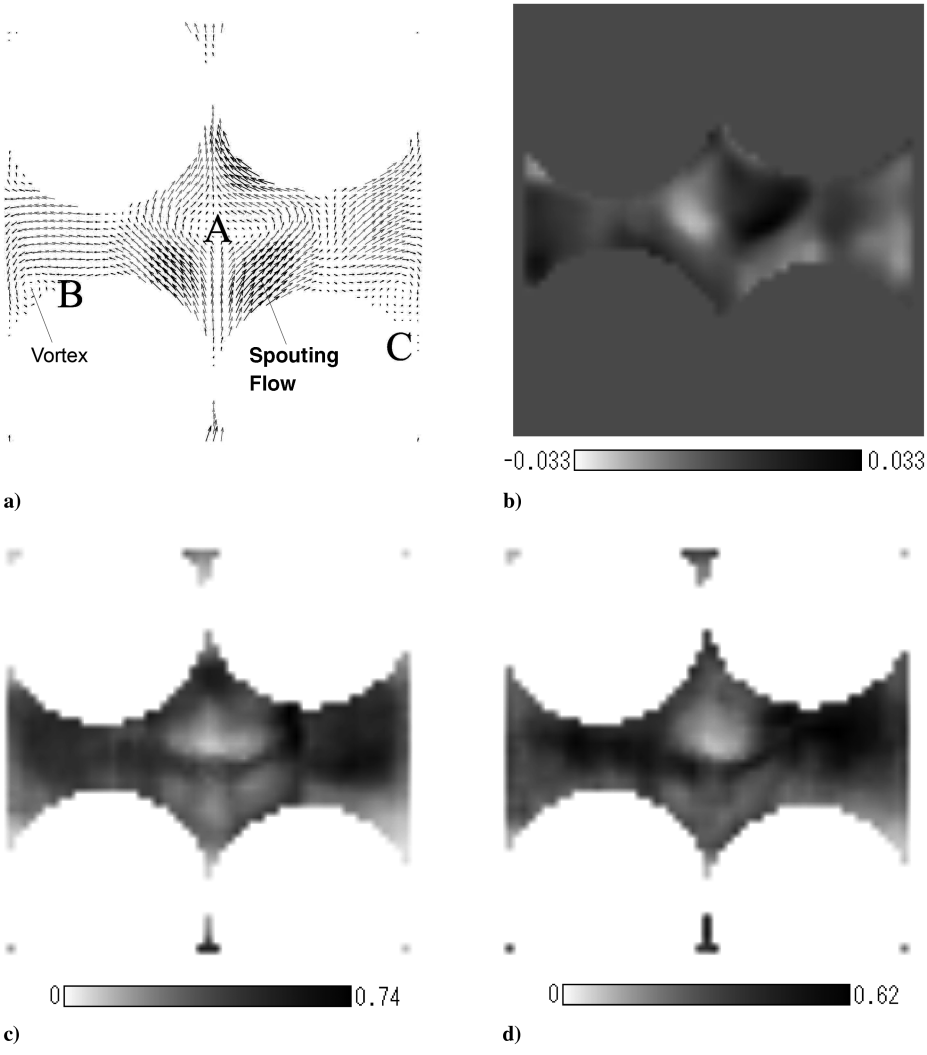

Fig. 9 Time-averaged flowfield, vorticity, and intensity of the velocity fluctuation ($Re_d = 800$).

impinging flow. An interesting feature is the formation of a low-velocity area in the middle of the spouting flow and the impinging flow, which seems to capture a coexisting area of different kinds of several flows in the SPP. In addition, there is stagnation in the area C closely located to the contact point between the sphere and the wall. It is impossible to remove enough heat in this area under the heating conditions, and so the wall temperature could rise sharply here, especially for the high Pr number fluid. However, the area downstream of this stagnation seems to have a high heat transfer performance due to the effect of the impinging flow. Figure 9b shows the vorticity distribution for the time-averaged flowfield. The regions around area A and near the wall with high vorticity hold a high heat transport performance. Hence, the spouting flow around the central area and its returning effect efficiently transport enthalpy that was transported from the heating wall by the circular vortex toward the center of the pipe, which could work more effectively if there existed active heat conduction from the wall to the sphere. Figures 9c and 9d, respectively, represent the intensities of the velocity fluctuation in the radial and streamwise directions, U_p and V_p, which are calculated by root mean square and normalized by each inlet velocity U. A strong velocity fluctuation area is formed upstream of the sphere existing downstream. This is the region where the spouting flow is pushed back by something strong flow colliding with the downstream sphere and branches again. Their maximum values over 0.6 indicate that the intensity of this variation is quite high. These fluctuations could significantly contribute to the heat transport from the wall, because both of the areas with high-velocity fluctuation spread toward the pipe wall.

Figure 10 shows distributions of the time-averaged flowfield, vorticity, and intensities of the velocity fluctuation in the radial and streamwise directions at $Re_d = 4900$. The instantaneous flowfields are not shown, as it is difficult to visually understand the difference from the $Re_d = 800$ case, though the unsteadiness of the flowfields seems to be much stronger. This leads to the fact that the circular vortex observed in area B of Fig. 9a becomes ambiguous with the increase in the Re_d number. It is confirmed that the high-velocity spouting flow observed around the central area is being prevented from spreading in a radial direction. Figure 11 presents two kinds of profiles at the horizontal center line of the visualizing area: one is the velocity profile about u and v in the radial and streamwise directions and the other is the intensity profiles of the velocity fluctuation U_p and V_p. The radial velocity near the wall indicates the strength of the impinging flow and is 1.0–1.5 times higher than the inlet velocity. The velocity profiles at $Re_d = 4900$ differ from the $Re_d = 800$ and 2000 cases and indicate a lower value, especially near the wall. This is because the impinging flow area moves further downstream at $Re_d = 4900$. As for the streamwise velocity profile, the spouting flow around the center area is accelerated as the Re_d number increases. Both figures show that the velocity peak position near $x/R = \pm 0.25$ shifts toward the center of the pipe with an increasing Re_d number, which proves the aforementioned prevention of the spread of the spouting flow and also suggests the development of something strong flow pushing the spouting flow back. Additionally, there are two areas with high-velocity fluctuation near $x/R = \pm 0.5$ for each Re_d number, which indicates that the aforementioned two characteristic flow structures themselves have strong variation and

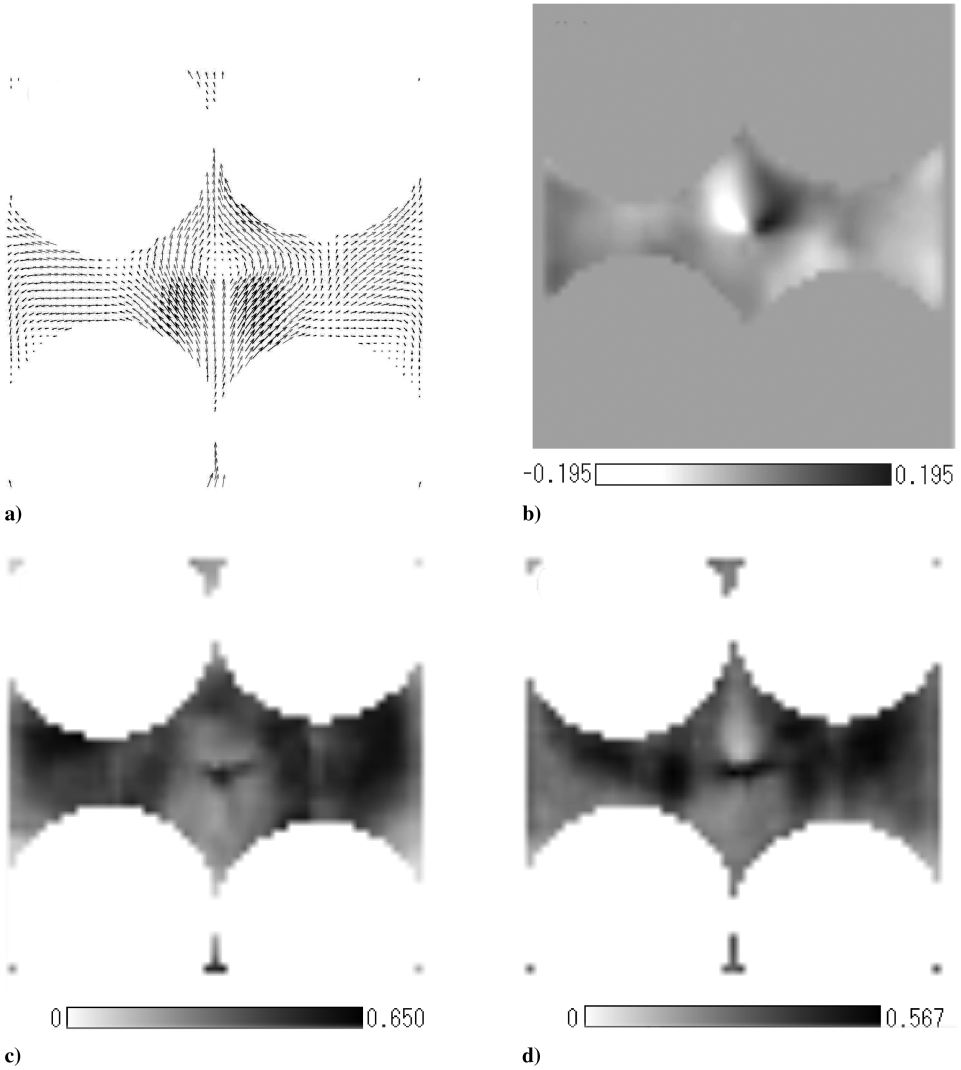

Fig. 10 Time-averaged flowfield, vorticity, and intensity of the velocity fluctuation ($Re_d = 4900$).

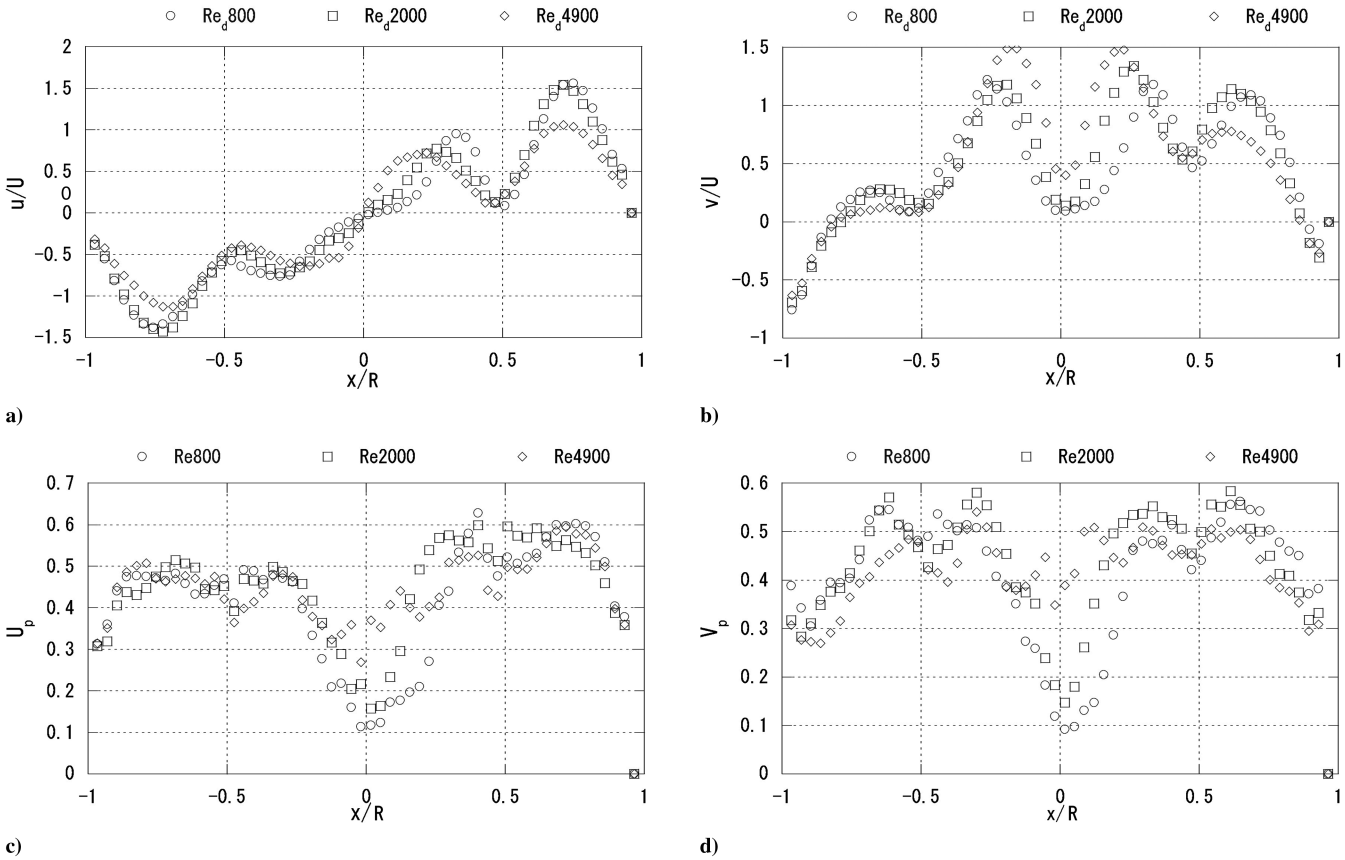

Fig. 11 Mean velocity and velocity fluctuation intensity profiles in the radial and streamwise directions.

are closely linking with each other because of the lack of significant difference in the variation of both the flow structures. In all data, there exist low flow velocity and a low-velocity fluctuation area at the location of $x/R = \pm 0.5$. This location corresponds to the coexistence area for the two flow structures that seems to exist around the right and left sides of the sphere existing in front and back of area A. The flow structure in this coexistence area will be clarified later by comparison with the flow structures on the other cross sections.

B. Flow Structure of Bypass Flow Due to Wall Effect

Because the present SPP has four wide gap channels in the streamwise direction due to the existence of the pipe wall, the flow characteristics of a high-velocity channeling flow, that is to say, a bypass flow formed in this area, strongly affect not only the flow structures of the spouting flow and the vortices behind the sphere but also the heat transfer characteristics. To capture this flow, a longitudinal section S_2, shown in Fig. 12, is visualized. Figures 13a–13d are the distributions of the time-averaged flowfield, vorticity, and intensities of the velocity fluctuation, respectively, in the right half area of S_2 at the Re_d of 800. The bypass flow flowing in parallel with the pipe wall is observed in the gap area between the sphere and the pipe wall. The wake area behind the sphere has a high vorticity, because the flow direction shifts to the back from the front of the paper depending on the packing structure. In addition, the intensities of the velocity fluctuation, U_p and V_p, are more overwhelmingly intense than those in the case of the aforementioned longitudinal section S_1, which indicates a strong unsteadiness of the flowfield in this section, especially beside and behind the sphere. A time series of the flowfields allows us to confirm that a circular vortex or a flow with low velocity is intermittently formed in this area (note: this is caused by a strong variation at the bend of the bypass flow described later on). Figure 14 shows the same distributions at $Re_d = 4900$. Although the flow velocity distribution and the vorticity distribution resemble those at $Re_d = 800$, the area with the high-velocity fluctuation behind the sphere expands more, showing a higher value in the intensity of the velocity fluctuation, especially in the radial direction. To quantitatively evaluate the influence of the Re_d number on the flow structure of the bypass flow, Figs. 15a–15d show the flow velocity profiles and the intensity profiles of the velocity fluctuation in the radial and streamwise directions at the horizontal center line in the middle of S_2. The minus value of the radial flow velocity means that the sphere shape contributes to a certain amount of momentum transfer toward the center of the pipe. Additionally, Fig. 15b shows that the bypass flow has quite a high velocity, whose maximum value is around 6 times that of the mean velocity. The Re_d number does not seem to affect the value much. Judging from this, it is evident that the bypass flow could be the something strong flow for the spouting flow being pushed back and for producing some vortices, including the impinging flow. Though the intensity of velocity fluctuation in both the radial and streamwise directions goes up as the Re_d number increases, the data at $Re_d = 800$ show a peculiar profile. It is considered that the flowfield at $Re_d = 800$ still has the characteristics of a lower Re_d number regime in which there exists a different kind of vortex shedding behind the sphere.

To evaluate the three-dimensional structure of the bypass flow, we focused on the flowfield in the longitudinal section S_3 perpendicular to S_2 is (see Fig. 16). Figures 17a–17d show the distributions of the

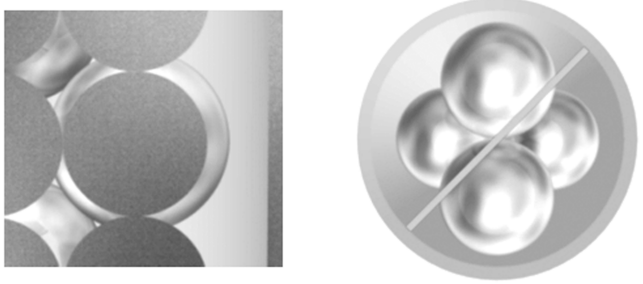

Fig. 12 Visualizing section: S_2.

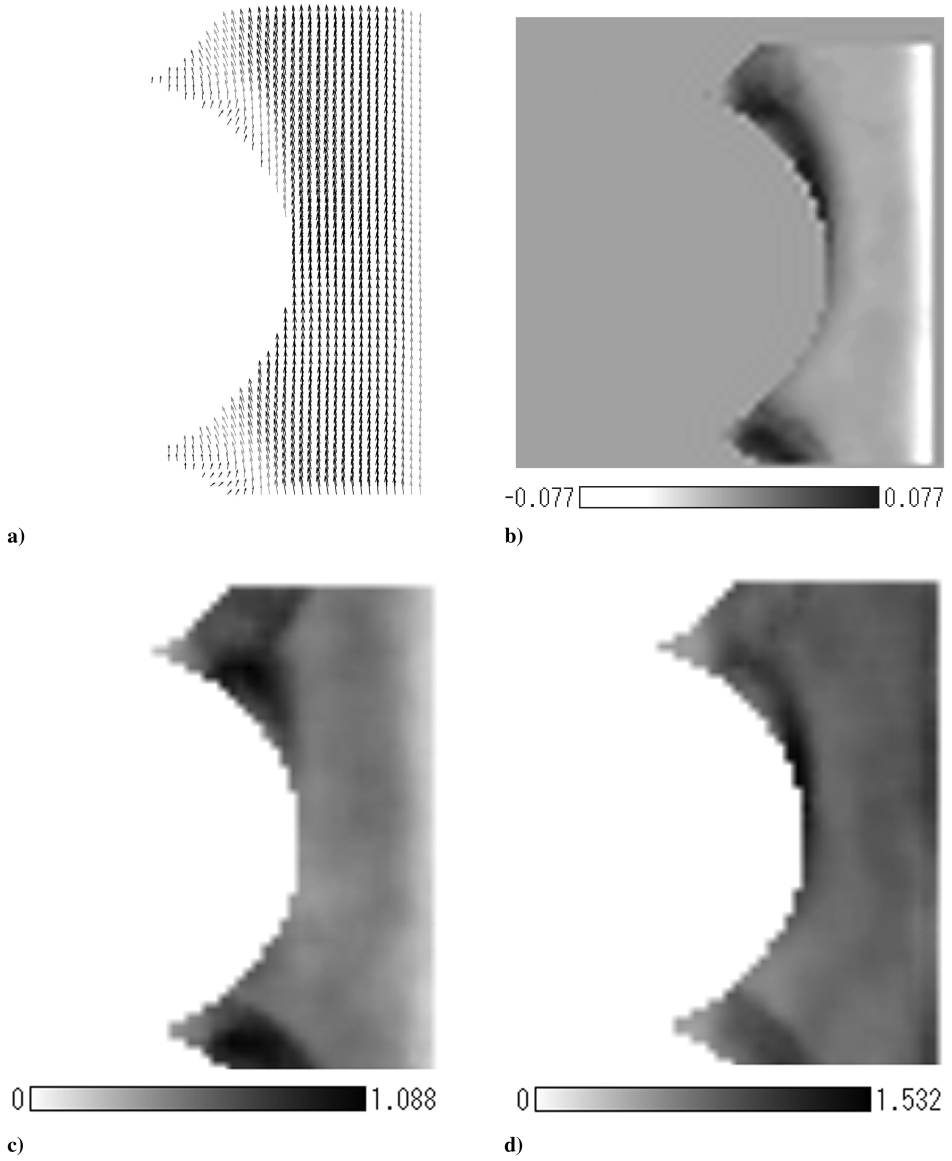

Fig. 13 Time-averaged flowfield, vorticity, and intensity of the velocity fluctuation of the bypass flow ($Re_d = 800$).

time-averaged flowfield, vorticity, and intensities of the velocity fluctuation in the horizontal and vertical directions (U_p and V_p) of the visualizing section at $Re_d = 800$. The bypass flow is flowing with a meandering motion through the spheres in a circumferential direction. Furthermore, a circular vortex is formed between the upstream and downstream spheres. As this circular vortex is formed near the downstream sphere, the flow that is branched by the meandering bypass flow colliding with the downstream sphere plays a significant role in forming the vortex. In addition, the existence of a high-vorticity area A being released from the sphere represents the boundary of the bypass-flow route. Regarding the velocity fluctuation U_p in the horizontal direction of S_3, the area with high-velocity fluctuation is formed on the bypass-flow route, which means that the bypass flow itself unsteadily changes in the circumferential direction. Furthermore, an area B with a high-velocity fluctuation is formed forward of the downstream sphere. As already described, a part of the bypass flow collides with the downstream sphere due to its meandering motion. In such areas, the flow becomes unstable and increases the intensity of the velocity fluctuation due to the influence of the sphere geometry. Regarding the intensity of the velocity fluctuation V_p in the vertical direction of S_3, an area C with a high-velocity fluctuation exists beside the bypass-flow route between the upstream and downstream spheres. The flow loses stability in this large gap area by being released from the influence of the upstream sphere surface, which could also lead to the formation of the impinging flow mentioned before, though this flow cannot be confirmed in section S_3. Figures 18a–18d also show the same distributions at $Re_d = 4900$. Figure 19 is a time series of the flowfields. Looked at through the time-averaged flowfield characteristics, the flow structures do not show as significant a change as in the $Re_d = 800$ case. However, the time series of the flowfields show that two apparent circular vortices are formed between the downstream and upstream spheres. In other words, the wake structure in the large gap area between the spheres is characterized by the coexistence of the circular vortex formed by the colliding effect of the bypass flow with the downstream sphere and by the separation vortex shedding from the upstream sphere. In particular, the small vortex shown in Fig. 8 corresponds to a part of this downstream vortex. The existence of these two vortices has been also confirmed at $Re_d = 800$. In the SPP flow, it is quite interesting that several vortices exist between the upstream and downstream spheres. In addition, the areas having a high vorticity and high-velocity fluctuation observed at $Re_d = 800$ spread in the circumferential and streamwise directions, which proves that the bypass flow meanders in a larger area with an increasing Re_d number. This fact can be confirmed by Figs. 20c and 20d, which show the intensities of the velocity fluctuation in the horizontal and vertical directions at the horizontal center line of S_3. In Fig. 20a, the

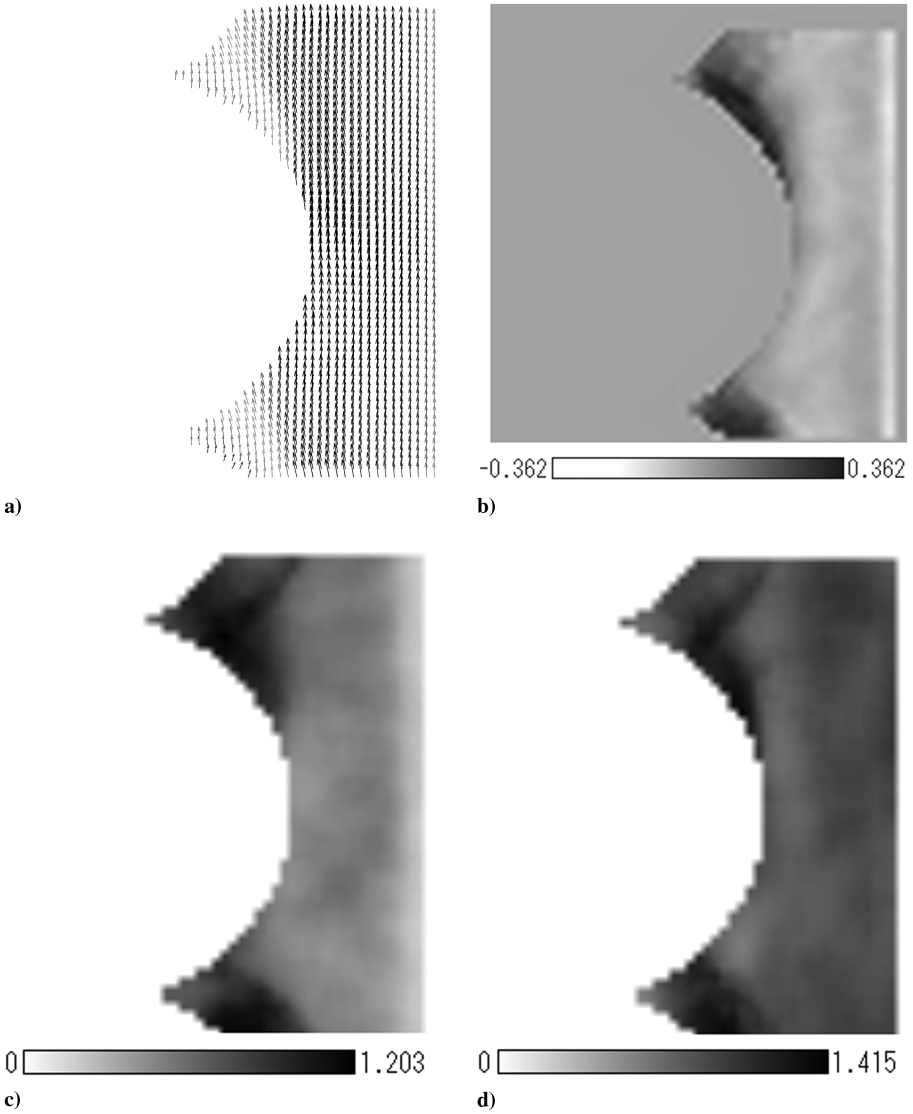

Fig. 14 Time-averaged flowfield, vorticity, and intensity of the velocity fluctuation of the bypass flow ($Re_d = 4900$).

horizontal velocity indicates a minus value because of the separation vortex near the wall. Observing the streamwise velocity profiles in Fig. 20b, the maximum flow velocity of the bypass flow is almost 5–6 times higher than the mean velocity, regardless of the Re_d number. This fact accords with the result shown in Fig. 15b. Moreover, the central axis of the bypass flow also seems not to be influenced by the Re_d number, because the peak location of the streamwise velocity does not shift with the change in the Re_d number.

C. Flow Structure Behind the Sphere

To further identify the wake structures formed between the spheres, the longitudinal section S_4, shown in Fig. 21, is visualized. Figure 22 is a time series of the flowfields at $Re_d = 4900$, and Figs. 23a–23c show the distributions of the vorticity and intensities of the velocity fluctuation in the horizontal and vertical directions of S_4, respectively. The high-velocity flow existing in the gap between the sphere and the pipe wall is the bypass flow itself. Observation using the time series of the flowfields confirms the generation and disappearance of a circular vortex, such as the Karman-like twin vortices behind the sphere, that is strongly affected by the inflowing of a part of the bypass flow. Because of this inflow, an area with high vorticity exists behind the sphere as shown in Fig. 23a. The shape and behavior of these vortices are another aspect of the aforementioned separation vortex. Though it is difficult to visualize both the upstream and downstream circular vortices simultaneously, the downstream circular vortex, which should also be twin vortices, seems to be somewhat flat in the circumferential direction and formed near the pipe wall as shown in Fig. 8. In addition, the gap area between the spheres has a high-velocity fluctuation; this also indicates the strong time variation of these two pairs of twin vortices. These vortices do not affect the bypass flow structure and its behavior significantly, because the area with the high-velocity fluctuation by the wake does not spread out to the bypass-flow area. To sum up, there are two factors that form the structure of the wake between the spheres and their unsteady behavior (see Fig. 23d, which illustrates the flow structures in S_3 and S_4): 1) twin separation vortices shedding from the sphere in a process whereby a part of each high-velocity bypass flow passing beside the sphere flows into the large gap area located behind the sphere (this process also generates the strong impinging flow mentioned later), and 2) twin circular vortices generated by the colliding and branching effects of two bypass flows in front of the downstream sphere.

D. Flow Structure in a Cross Section of Circular Pipe

Finally, the flowfields in a lateral cross section of the pipe, that is, a secondary flow, are visualized to investigate the three-dimensional structure of the flowfield in the SPP. Figures 24 and 25, respectively, show a time series of the secondary flows at the Re_d numbers of 800 and 4900 in the cross section S_5 perpendicular to the longitudinal section S_1 (see the first figure in Fig. 26). The last figures in Figs. 24 and 25 show the time-averaged flowfield. Figure 26 shows the distributions of the vorticity and the intensities of the velocity

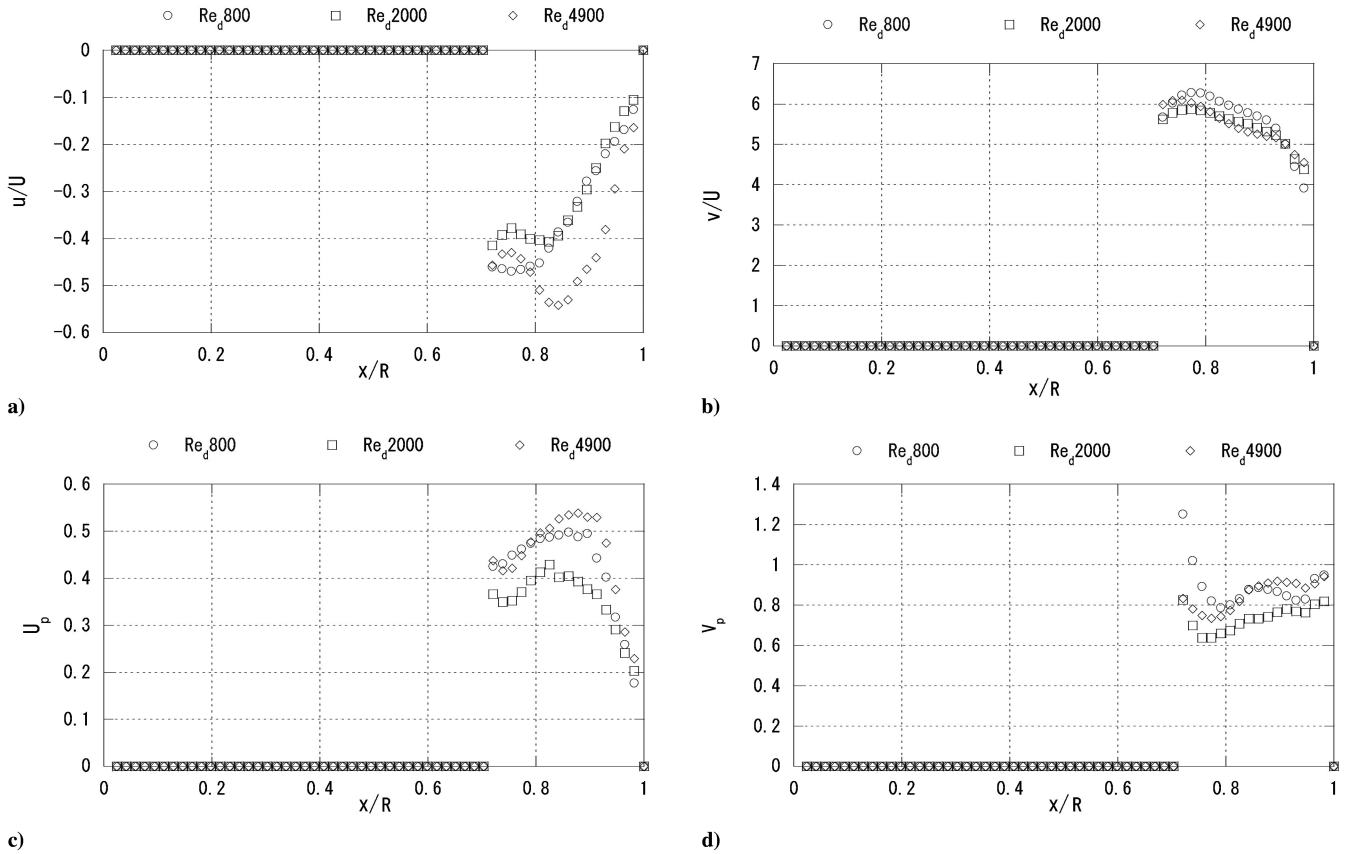

Fig. 15 Mean velocity and velocity fluctuation intensity profiles in the radial and streamwise directions.

fluctuation in the horizontal and vertical directions of S_5 at $Re_d = 4900$. These figures clearly show that apparent twin vortices with strong variation exist in the lateral cross section. The four circled areas show the ones through which the bypass flow passes. As already mentioned, the bypass flow meanders along the sphere geometry and a part of it flows into the large gap area between the upstream and downstream spheres, and so it is obvious that the bypass flow becomes a significant driving flow for the twin vortices. Additionally, the strong flow toward the wall, which is in the middle of the twin vortices, corresponds to the impinging flow confirmed in cross section S_1. In other words, the two bypass flows heading toward the large gap area, after passing through the upstream sphere, generate the twin vortices that correspond to the upstream separation vortices. Because there is one more pair of twin vortices downstream due to the colliding effect of the two bypass flows with the downstream sphere, these two different twin vortices form three-dimensional structures in the gap area. On the other hand, the velocity vectors of the spouting flow from the pipe center observed in the cross section S_1 have not been confirmed. It is predicted that the bypass flow toward the gap area pushes back the spouting flow toward the pipe center again in section S_5. As a result, the low-velocity area in the upstream of the impinging flow is formed as shown in the last vector diagrams of Figs. 24 and 25. Although the spouting flow also tries to spread out in a circumferential direction, it heads toward the opposite direction against the rotating direction of the twin vortices.

The multiple vortices with the aforementioned complex structure could have strong effects on the fluid mixing and heat transport from the heating wall, which suggests that control of the bypass flow plays an important role in the heat transfer augmentation of the SPP.

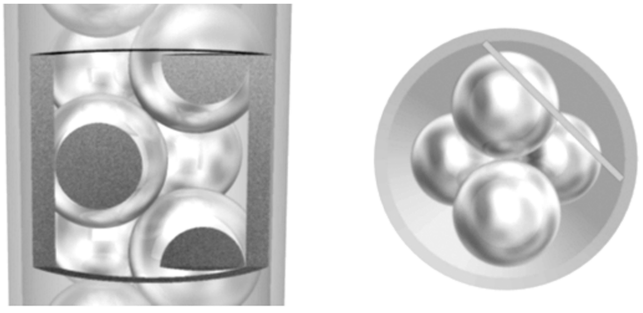

Fig. 16 Visualizing section: S_3.

IV. Heat Transfer Characteristics of a Sphere-Packed Pipe Flow

A. Wall-Temperature Distribution and Local Heat Transfer Characteristics

Figures 27a and 27b show the inner wall temperatures of the heating circular pipe, which are estimated by Eq. (3) using outer wall-temperature data from nos. 4 to 11 shown in Fig. 6. The flow conditions are at $Re_d = 800$ and 4900, and the figure shows both the high heat flux (700 A) and low heat flux (500 A) cases. The axis of the abscissa is the length from the start position of heating. The data show significant temperature differences among the three thermocouples located at the same axial position. Especially in the case of high heat flux at $Re_d = 800$, a maximum 23° of temperature difference can be confirmed at the position of $z = 475$ mm (no. 10). One of these thermocouples is located near the contact point of the sphere and the pipe wall, at the position where such a significant temperature difference can be measured. The visualization experiment has shown that the area around this point is the stagnation area of the flow, and not enough heat transfer sharply rises the wall temperature in this area. However, the colliding effect of the bypass flow with the spheres also seems to enhance the heat transfer performance at this point because the temperature difference decreases as the Re_d number increases (maximum 5° at $Re_d = 4900$). On the other hand, there is also the axial position showing a low temperature difference with a low wall temperature (e.g., $z = 225$ mm at no. 5). At this position, the thermocouples are

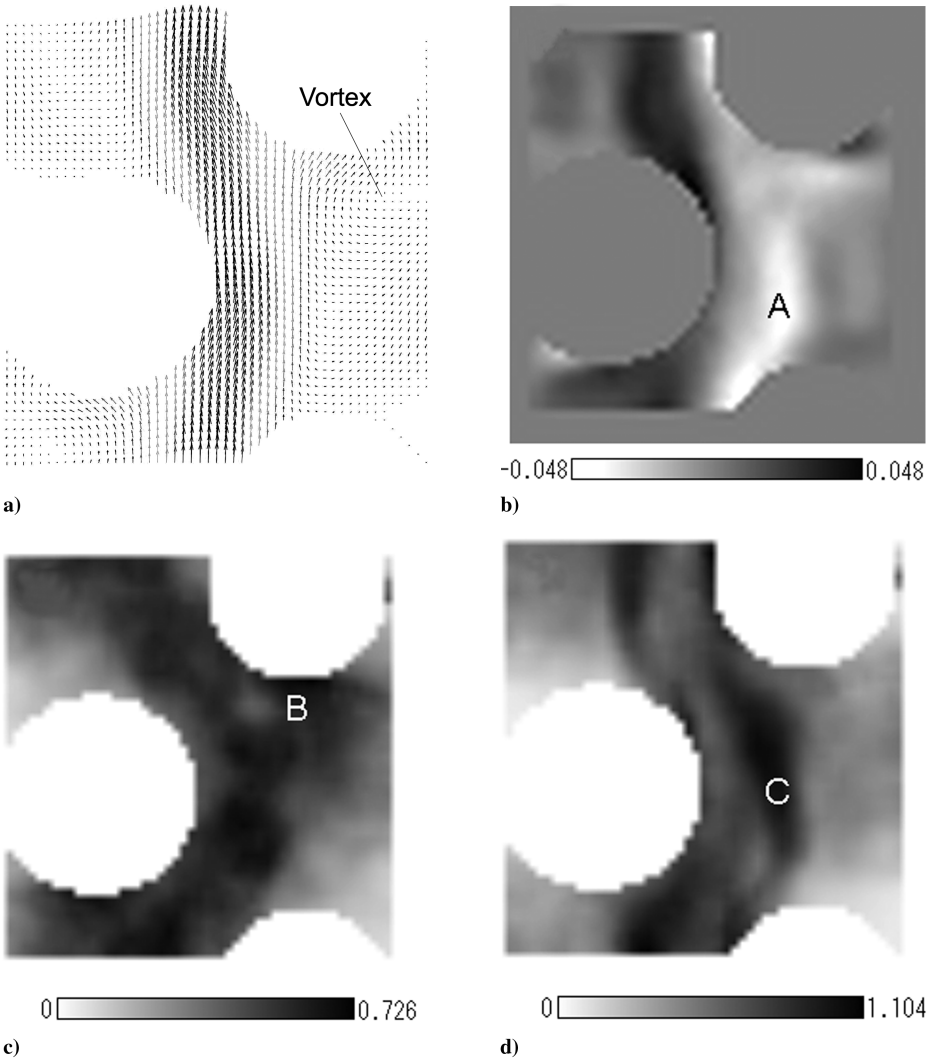

Fig. 17 Time-averaged flowfield, vorticity, and intensity of the velocity fluctuation of the bypass flow ($Re_d = 800$).

attached slightly upstream of the contact point. In this area, there exists the strong impinging flow toward the pipe wall and the downstream twin vortices, and so this proves that these flows significantly contribute to the heat transfer enhancement. Figure 28 shows the distributions of the local heat transfer coefficients. The local heat transfer coefficients at $Re_d = 4900$ are approximately 3 times higher than those at $Re_d = 800$. A solid line in the figure shows the average heat transfer coefficient estimated by the following Varahasamy and Fand's correlation [11]:

$$h = CRe_D^m(Pr^p)(f_w Re_w)^q[\tan^{-1}(D/d)^n]^r(k_{\text{eff}}/D) \qquad (4)$$

In this correlation, Re_w is the wall-modified Reynolds number, and C, m, n, p, q, and r are constants that are fixed according to a value of D/d and the flow conditions. Although the size ($D/d = 2.0$) of the sphere is basically inapplicable to Varahasamy and Fand's correlation, each constant is adopted under the conditions of $D/d > 3.0$ as a matter of convenience. Furthermore, Varahasamy and Fand defined effective thermal conductivity k_{eff} using a porosity and a thermal-conductivity ratio of fluid to sphere material. However, it is impossible to strictly define the effective thermal conductivity in the case of a low-thermal-conductivity material such as the acrylic sphere used in this experiment. This analysis adopted the thermal conductivity of water as the effective thermal conductivity, assuming that almost no heat conduction from the heating wall to the acrylic sphere exists at the contact point. In each flow condition, the local heat transfer coefficients disperse around Varahasamy and Fand's correlation, though the experimental data on average seem to be higher than Varahasamy and Fand's correlation. This means that it is possible to apply Varahasamy and Fand's correlation for roughly predicting the heat transfer performance and constructing a new correlation applicable to the $D/2.0$ size of the sphere-packed pipe with regularity.

To discuss the heat transfer performance of the SPP flow by using visually apparent wall-temperature distribution, thermal imagery by infrared thermography is shown in Fig. 29. The inside sphere-packed structure is also shown on the right-hand side, corresponding to the visualization area. The thermal imagery indicates that the Re_d number is 800 under high heat flux. It can be clearly observed that the crescent-shaped area with the high temperature is formed in the downstream of each contact point between the sphere and the pipe wall. This is due to the formation of the stagnation, which was observed around the contact point in the PIV measurement. Characteristically, the incurvation area with the high temperature caused by the bypass flow's meandering motion is obviously captured. The reason the bypass flow has a comparatively high temperature is thought to be because the velocity fluctuation caused by the colliding effect of the bypass flow with the spheres transports the heat stagnating around the contact point. Therefore, it is evident that the velocity fluctuation due to the colliding effect makes the wall-temperature distribution more uniform with the increase in the Re_d number. On the other hand, the crescent-shaped areas with the low temperature are also clearly observed in the large gap areas. Because the pipe wall generates heat uniformly, these low-temperature areas indicate that the heat is effectively removed and

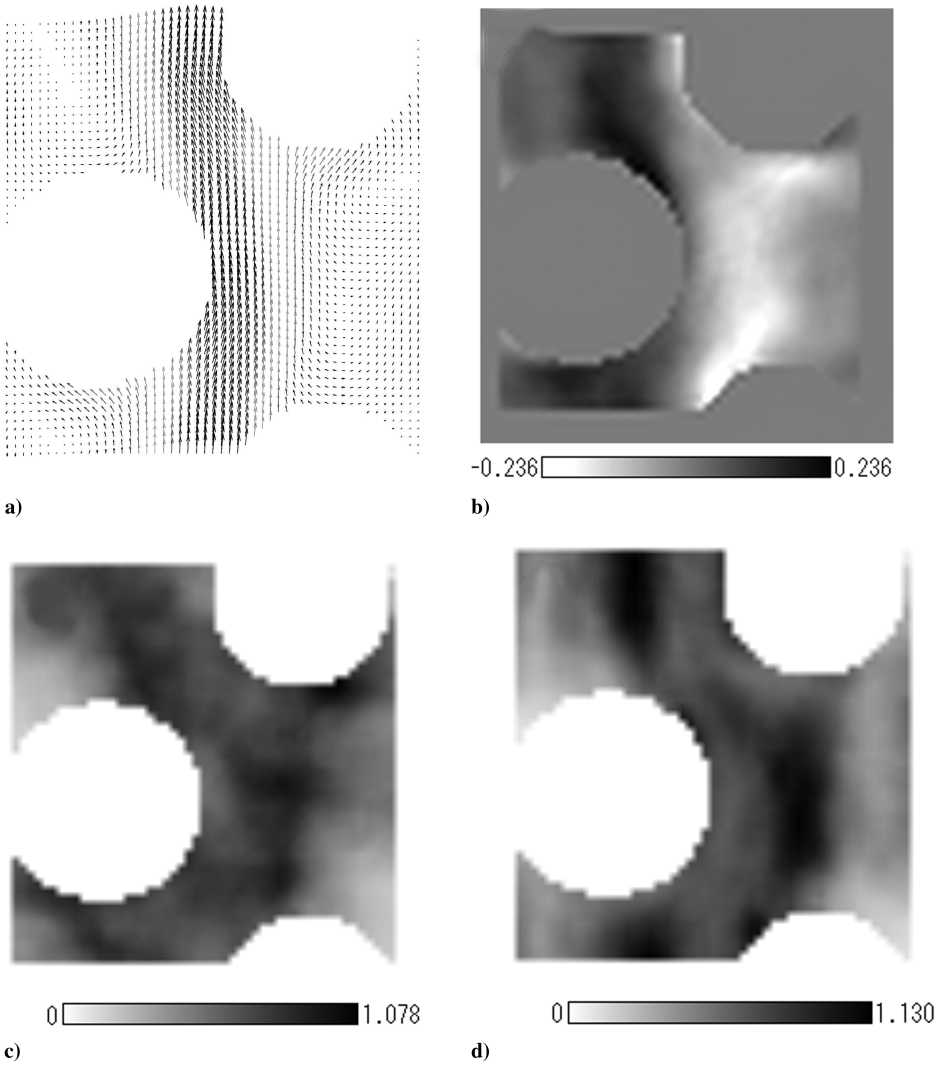

Fig. 18 Time-averaged flowfield, vorticity, and intensity of the velocity fluctuation of the bypass flow ($Re_d = 4900$).

transported in these areas. It seems that the branching circular vortices and the strong impinging flow contribute to the heat transfer enhancement in a wider area than expected.

B. Average Heat Transfer Performance of the SPP Flow

It is important to compare the heat transfer performance of the SPP flow with other typical heat transfer promoters. However, it is difficult to identify a fully developed region for the temperature field due to the dispersion of the wall-temperature data. Therefore, following Varahasamy and Fand's knowledge [11], an average heat transfer coefficient is evaluated by setting the region $z > 3.0D$ as the fully developed region for the temperature field. Figure 30 shows the characteristics of the average heat transfer coefficients for the inlet flow velocity. The heat transfer performance of the SPP flow is enhanced as the flow velocity increases. An error bar lengthens with

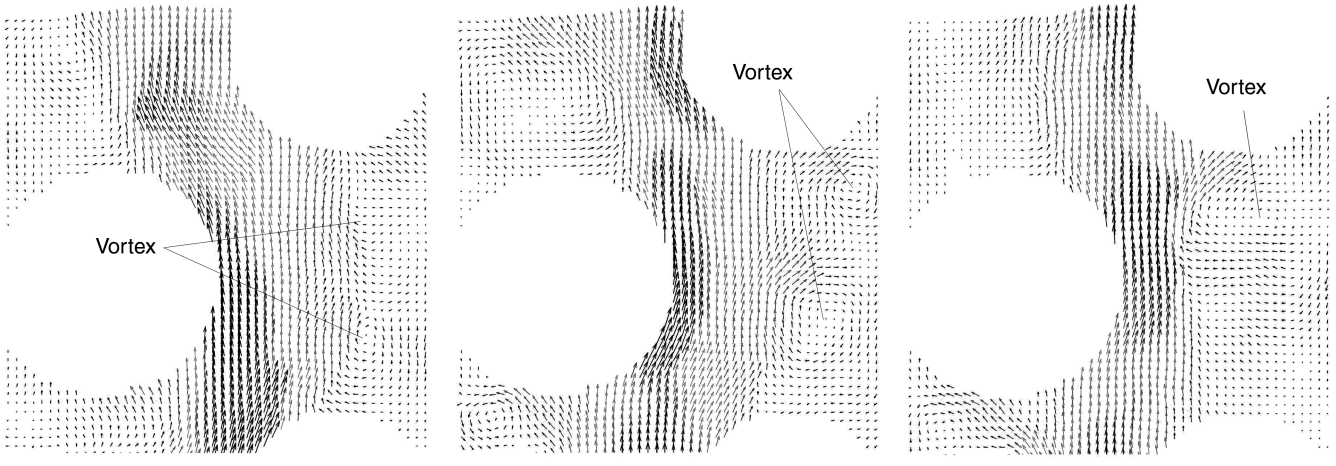

Fig. 19 Time sequence of the flowfields of the bypass flow ($Re_d = 4900$, time interval = 0.07 s).

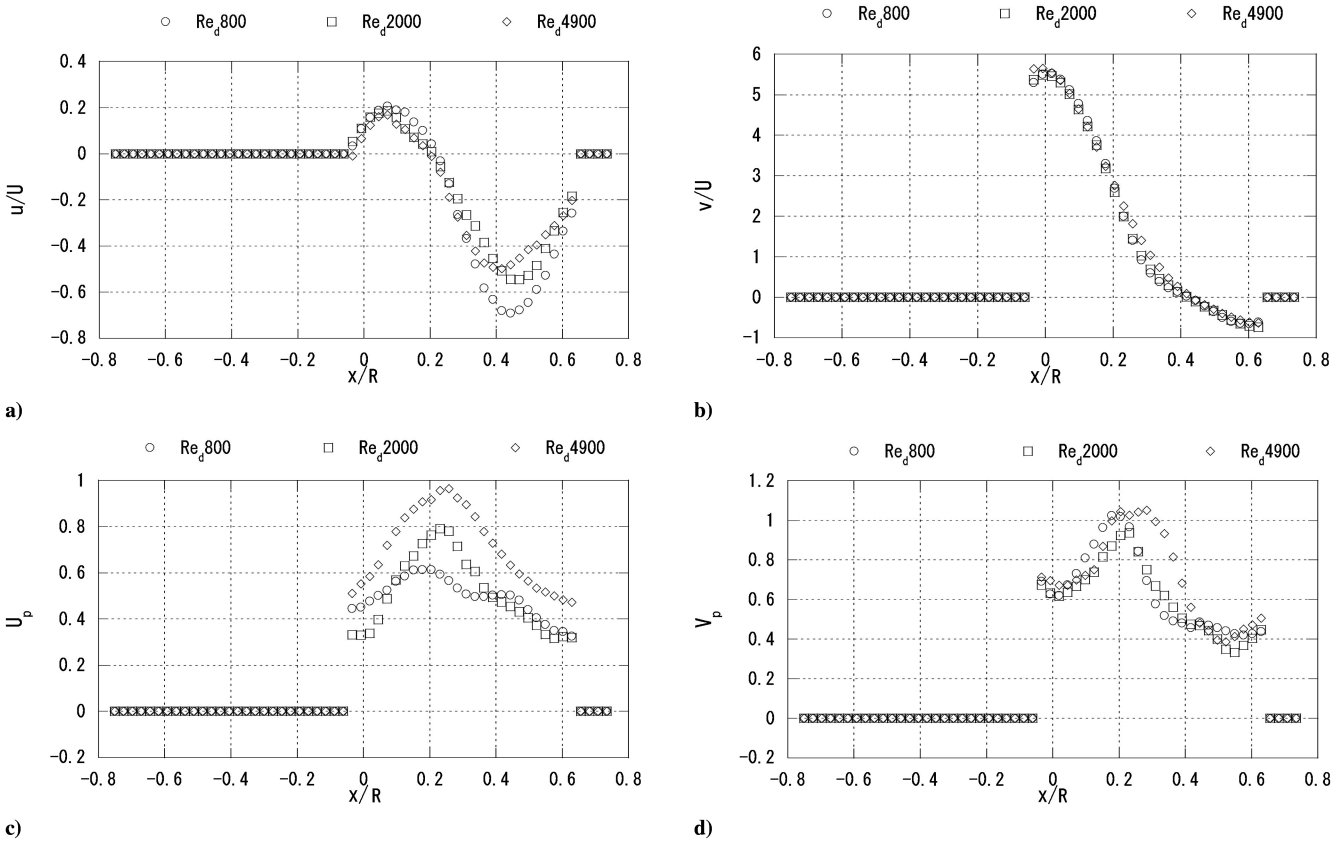

Fig. 20 Mean velocity and velocity fluctuation intensity profiles in the horizontal and vertical directions of S_3.

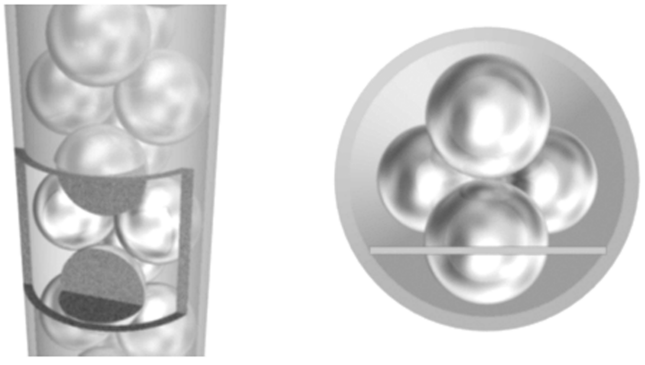

Fig. 21 Visualizing section: S_4.

the increase in flow velocity, which absolutely proves that flattening the wall-temperature distribution will be a key issue of developing advanced sphere-packed pipes for a high Pr number fluid. However, the heat transfer coefficients of the SPP flow are much higher, even compared with that of a twisted-tape-inserted pipe flow [13], that is, a swirl flow, with the twisted ratio of 3.0, as well as that of a smooth circular-pipe flow estimated by the Petukhov–Gnielinski's correlation. For instance, at the inlet Reynolds number of $Re_D = 10,000$ ($U = 0.16$ m/s), the heat transfer coefficient in the SPP flow is 5.3 times higher than that of the smooth circular-pipe flow and 3.9 times higher than that of the swirl flow (at $Re_D = 20,000$ ($U = 0.32$ m/s), it is 3.8 and 2.8 times higher, respectively), which means that it can accomplish an objective heat transfer coefficient under lower flow rate conditions. On the other hand, it is common knowledge that heat transfer enhancement technology has a tradeoff

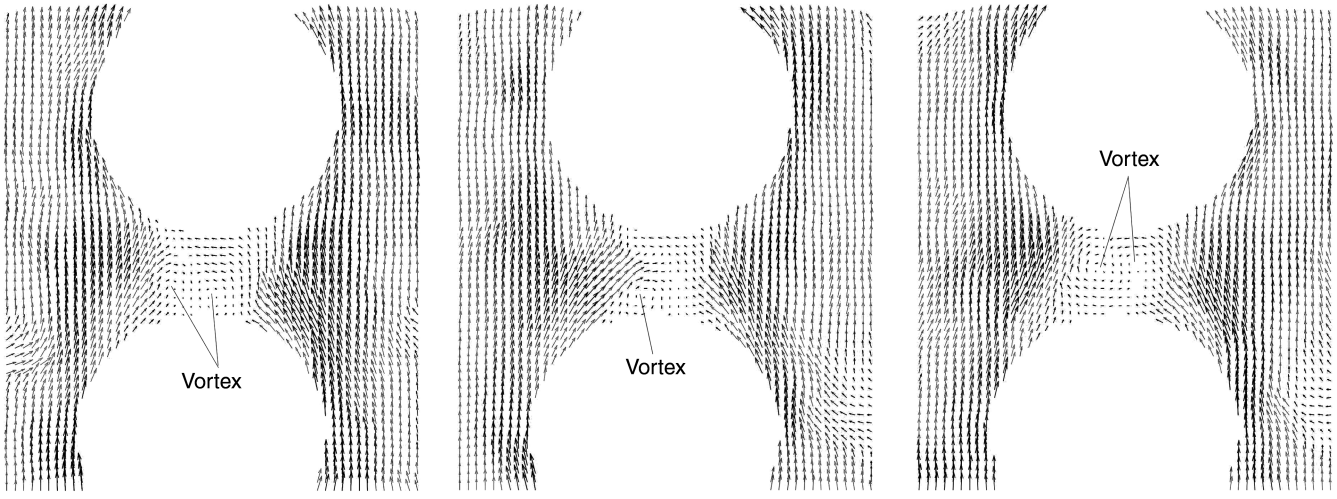

Fig. 22 A time series of flowfields behind the sphere ($Re_d = 4900$, time interval = 0.07 s).

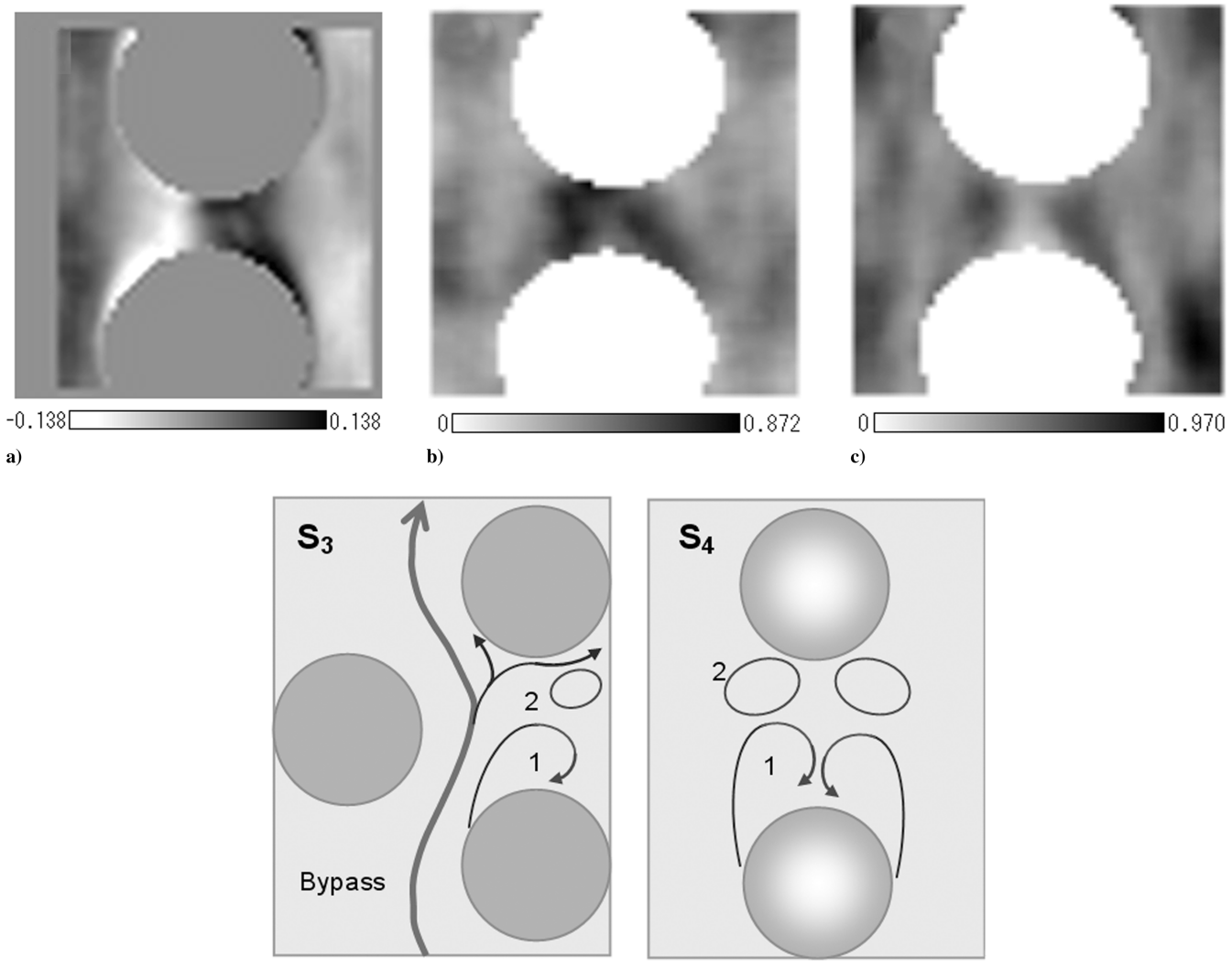

Fig. 23 Vorticity and velocity fluctuations ($Re_d = 4900$), and an illustration of the flow structure in S_3 and S_4.

relation with pressure-drop increase. In most cases, the heat transfer efficiency (which equals the rate of heat transfer enhancement times the rate of pressure-drop increase) shows up at much less than 1.0. Naturally, there is fear for the SPP that a tremendous increase in the pressure drop appears due to packing too many obstacles in the circular pipe. Figure 31 shows the characteristics of the average heat transfer coefficients of the SPP flow for the pressure drop $\Delta P/L$. Under the same pressure-drop conditions, the heat transfer performance of the circular-pipe flow is more than 4 times as high as that of the SPP flow under all of the flow rate conditions. Actually, the heat transfer efficiencies at $Re_D = 10,000$ and 20,000 indicate very low values, respectively. However, the most important thing in actual plant design is to compare the heat transfer performance with the pumping power. Especially when giving consideration to all of the pressure drops for a piping system consisting of a lot of components and/or bends, etc., a heat transfer promoter with higher heat removal performance under lower flow velocity conditions could be also applicable from the viewpoints of reduction in electrolysis, MHD pressure drop, and erosion. Figure 32 shows the influence of pumping power $P_{\text{pump}}[\text{W/m}] = Q[\text{m}^3/\text{s}]^* \Delta P/L$ on the heat transfer performance. It shows that, under the conditions of $P_{\text{pump}} < 0.3$ W/m, the heat transfer coefficients of the SPP flow are

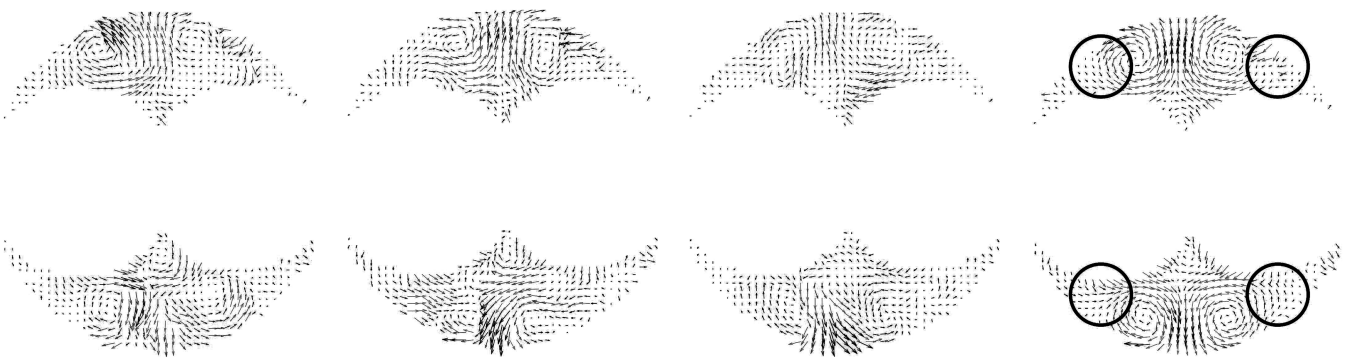

Fig. 24 A time series of secondary flows ($Re_d = 800$, time interval = 0.07 s).

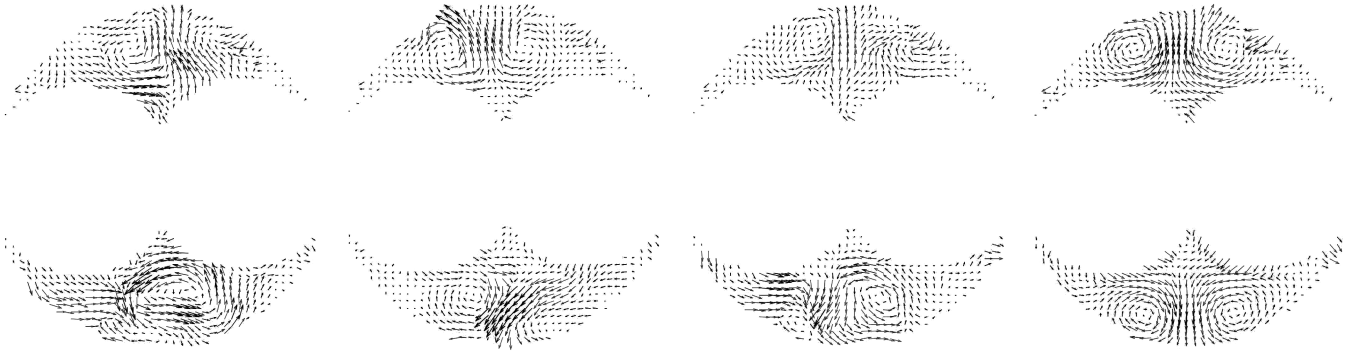

Fig. 25 A time series of secondary flows (Re_d = 4900, time interval = 0.07 s).

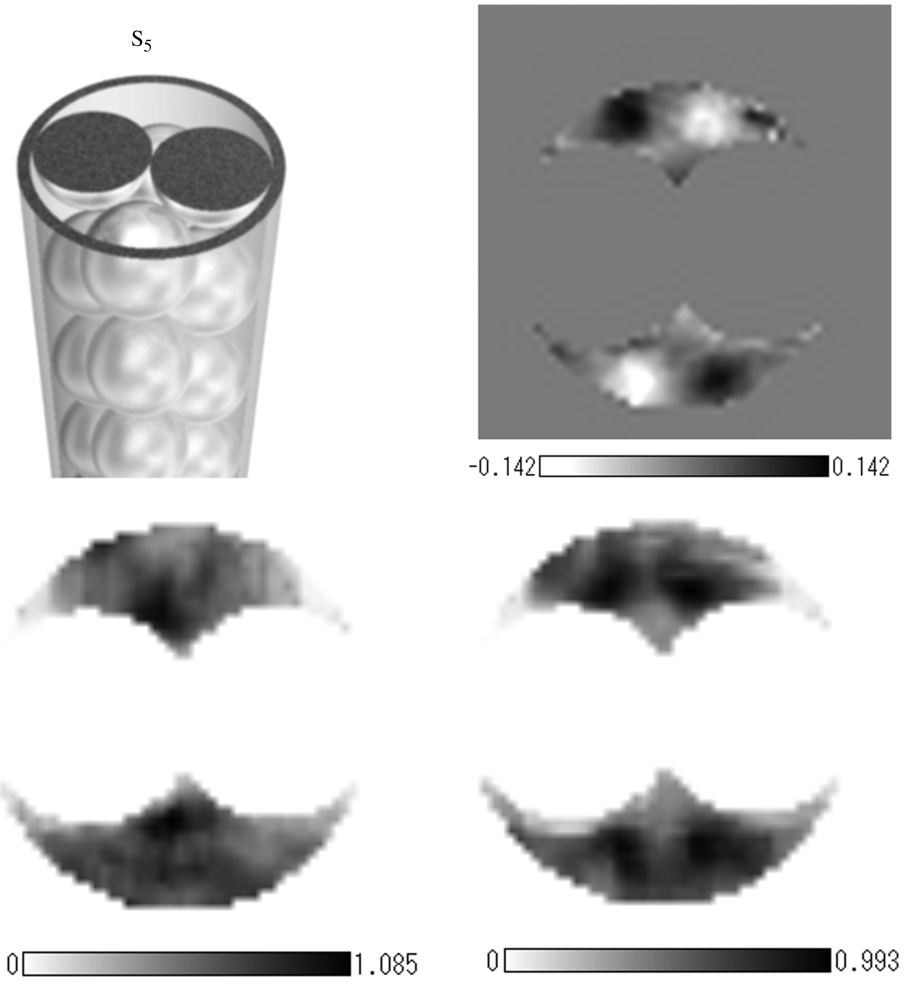

Fig. 26 Distributions of the vorticity and intensities of the velocity fluctuation at Re_d = 4900.

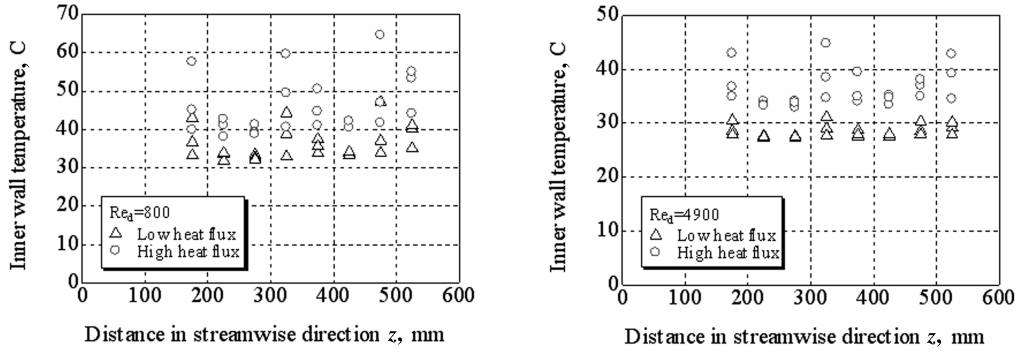

a) b)

Fig. 27 Distributions of the wall temperatures of the sphere-packed pipe (Re_d = 800 and 4900).

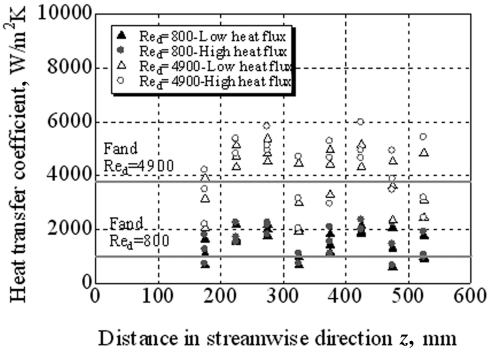

Fig. 28 Distributions of the heat transfer coefficients.

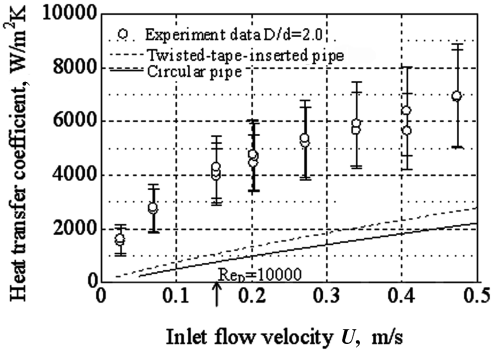

Fig. 30 Effect of the flow velocity on the heat transfer coefficients.

higher than that of the circular-pipe flow. This means that the SPP is especially effective under lower pumping power conditions. However, the heat transfer performance of the SPP flow at $P_{\text{pump}} > 0.3$ W/m is lower than that of the circular-pipe flow, and almost half at $P_{\text{pump}} = 15$ W/m, which surely suggests that it needs to dramatically enhance the heat transfer performance by improving the fin effect from the heating wall to the sphere and changing the packing structure, etc., when using a sphere of $D/2.0$ in diameter. For reference, the heat transfer performances for the different sphere sizes, $D/d = 3.0$ and 1.4, are also shown in the same figure, using of the Fand's correlation. Although there are some problems with using the Fand's correlation, especially for a high Re_d number regime, the use of smaller-size spheres seems to be much more effective than the $D/2.0$-size sphere in the case without the fin effect. In addition, the pipe diameter $D = 56$ mm in this experiment is quite large for the piping in the fusion reactor, and so the scale effect for the heat transfer coefficient is available when using a smaller-diameter pipe, which would lead to an effective use of the SPP under the aforementioned superior conditions. These evaluations prove the high potential of the sphere-packed pipe as a heat transfer promoter for the molten salt blanket system in a fusion reactor. (For more information on this, refer to Sato and Yuki [14].)

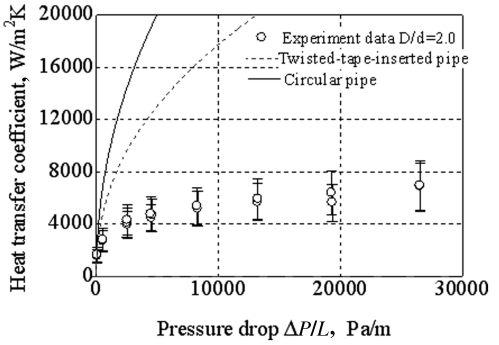

Fig. 31 Effect of pressure loss on the heat transfer coefficients.

V. Conclusions

In this study, PIV visualization was performed to understand the complex flow structures in a sphere-packed pipe. The PIV experiment was conducted using a matched refractive-index method with NaI solution as the working fluid. Then, through heat transfer experiments, the wall-temperature distribution was measured with thermocouples and infrared thermography, which made clear the relation between the flow structures and the local heat transfer performance. The knowledge obtained is summarized as follows:

1) As representative flow structures in a sphere-packed pipe, the following three flows were confirmed: a meandrous bypass flow with high-flow velocity due to the wall effect, two pairs of twin vortices accompanied with a strong impinging flow to the wall, and a spouting flow from the central area of the pipe.

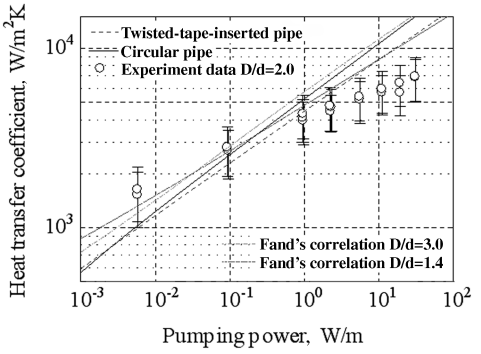

Fig. 32 Effect of pump power on the heat transfer coefficient of SPP flows.

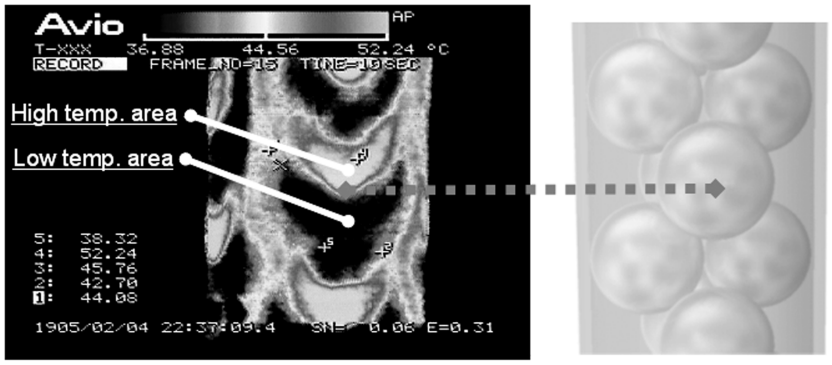

Fig. 29 Wall-temperature distribution ($Re_d = 800$).

2) An area with a high wall temperature is formed by the flow stagnation located around a contact point between the sphere and the heating wall.

3) The heat transfer performance is quite high in a large gap area between the upstream and downstream spheres, due to the influences of the impinging flow and the downstream twin vortices.

4) The colliding effect of the high-velocity, meandering bypass flow with the spheres significantly affects the heat transport from the stagnation areas.

If it is possible to optimize the packing structure to disarrange the bypass flow more structurally and to develop a heat-conduction enhancement technique at the contact point between the sphere and the pipe wall, it will be possible to achieve much higher heat transfer performance due to the multiplier functions of the fluid mixing effect near the heating wall and the fin effect, which enable the flattening of the wall-temperature distribution. It is also necessary to evaluate the change of the flow structures and the augmentation/suppression of the heat transfer performance under the magnetic field, after which these evaluations should be reflected in the design guide for the first wall of FFHR.

Acknowledgment

This work was performed with the support and under the auspices of the National Institute for Fusion Science collaborative research program (NIFS06KFDA007). We wish to acknowledge their support and assistance to our work.

References

[1] Sagara, A., and Imagawa, S., "Carbon Tiles as Spectral-Shifter for Long-Life Liquid Blanket in LHD-Type Reactor FFHR," *Fusion Engineering and Design*, Vol. 81, Nos. 8–14, Feb. 2006, pp. 1299–1304. doi:10.1016/j.fusengdes.2005.09.067

[2] Kobayashi, T., and Yuki, K., "Effect of Electrolysis on High Temperature Molten Salt Flow in a Magnetic Field," *Proceedings of the 17th ANS Topical Meeting on the Technology of Fusion Energy*, American Nuclear Society, La Grange Park, IL, 2006.

[3] Toda, S., Chiba, S., and Yuki, K., "Experimental Research on Molten Salt Thermofluid Technology Using a High-Temperature Molten Salt Loop Applied for a Fusion Reactor Flibe Blanket," *Fusion Engineering and Design*, Vols. 63–64, Dec. 2002, pp. 405–409. doi:10.1016/S0920-3796(02)00195-3

[4] Chiba, S., Omae, M., and Yuki, K., "Experimental Research on Heat Transfer Enhancement for High Prandtl-Number Fluid," *Fusion Science and Technology*, Vol. 47, No. 3, 2005, pp. 569–573.

[5] Okumura, M., and Yuki, K., "Evaluation of Flow Structure in Packed-Bed Tube by Visualization Experiment," *Fusion Science and Technology*, Vol. 47, No. 4, 2005, pp. 1089–1093.

[6] Ergun, S., "Fluid Flow Through Packed Columns," *Chemical Engineering Progress*, Vol. 48, No. 2, 1952, pp. 89–94.

[7] Watanabe, H. J., "Comment on Izbash Equation," *Journal of Hydrology*, Vol. 58, Nos. 3–4, 1982, pp. 389–397.

[8] Fand, R. M., and Thinakaran, R., "The Influence of the Wall on Flow Through Pipes Packed with Spheres" *Journal of Fluids Engineering*, Vol. 112, No. 1, 1990, pp. 84–88. doi:10.1115/1.2909373

[9] Fand, R. M., Sundaram, M., and Varahasamy, M., "Incompressible Fluid Flow Through Pipes Packed with Spheres at Low Dimension Ratios," *Journal of Fluids Engineering*, Vol. 115, 1993, pp. 169–172. doi:10.1115/1.2910102

[10] Fand, R. M., Varahasamy, M., and Greer, L. S., "Empirical Correlation Equations for Heat Transfer by Forced Convection from Cylinders Embedded in Porous Media that Account for the Wall Effect and Dispersion," *International Journal of Heat and Mass Transfer*, Vol. 36, No. 18, 1993, pp. 4407–4418. doi:10.1016/0017-9310(93)90125-P

[11] Varahasamy, M., and Fand, R. M., "Heat Transfer by Forced Convection in Pipes Packed with Porous Media Whose Matrices are Composed of Spheres," *International Journal of Heat and Mass Transfer*, Vol. 39, No. 18, 1996, pp. 3931–3947. doi:10.1016/0017-9310(96)00032-4

[12] Nematollahi, M. R., Toda, S., Hashizume, H., and Yuki, K., "Vibration Characteristic of Heated Rod Induced Flow Boiling," *Journal of Nuclear Science and Technology*, Vol. 36, No. 7, 1999, pp. 575–583. doi:10.3327/jnst.36.575

[13] Manglik, R. M., and Bergles, A. E., "Heat Transfer and Pressure Drop Correlations for Twisted-Tape Inserts in Isothermal Tubes Part 2: Transition and Turbulent Flows, *Transactions of the ASME: Journal of Heat Transfer*, Vol. 115, No. 4, 1993, pp 890–896. doi:10.1115/1.2911384

[14] Sato, T., and Yuki, K., "Heat Transfer Performance for High Prandtl and High Temperature Molten Salt Flow in Sphere-Packed Pipes," *Fusion Science and Technology*, Vol. 47, No. 4, 2007, pp. 1089–1093.